



Structure and phase regulation in Mo_xC ($\alpha\text{-MoC}_{1-x}/\beta\text{-Mo}_2\text{C}$) to enhance hydrogen evolution



Xiangyong Zhang^a, Junchao Wang^a, Ting Guo^a, Tianying Liu^a, Zhuangzhi Wu^{a,b,*}, Luigi Cavallo^c, Zhen Cao^{c,**}, Dezhi Wang^{a,b,*}

^a School of Materials Science and Engineering, Central South University, Changsha, 410083, China

^b Key Laboratory of Ministry of Education for Non-ferrous Materials Science and Engineering, Changsha, 410083, China

^c KAUST Catalysis Center, King Abdullah University of Science and Technology (KAUST), Thuwal 23955-6900, Saudi Arabia

ARTICLE INFO

Keywords:

Molybdenum carbide
Electrochemical catalyst
Hydrogen evolution reaction
Heterostructure

ABSTRACT

Non-precious metal-based efficient electrocatalysts with superior activity and stability for the hydrogen evolution reaction (HER) are useful in solving energy and environmental crises. Herein, monodisperse inverse opal-like Mo_xC ($\alpha\text{-MoC}_{1-x}/\beta\text{-Mo}_2\text{C}$) nanospheres were synthesized via a facile strategy to adjust the intrinsic activity and maximize the exposed active sites. In particular, the $\text{Mo}_x\text{C}-0.4$ with the optimal composition of $\alpha\text{-MoC}_{1-x}/\beta\text{-Mo}_2\text{C}$ (0.56/0.44) demonstrated a superior HER performance in 0.5 M H_2SO_4 with a small Tafel slope of 48 mV dec⁻¹ and remarkable stability. Such prominent performance not only benefits from the inverse opal-like structure that provides more active sites for HER, but also should be ascribed to the strong synergistic effect between $\alpha\text{-MoC}_{1-x}$ and $\beta\text{-Mo}_2\text{C}$. Based on theoretical calculations, it is further verified that the synergistic effect of $\text{Mo}_x\text{C}-0.4$ is originated from the optimization of interaction with the H^* induced by the heterostructure. Furthermore, this work will broaden our vision for highly efficient hydrogen production by bridging the microscopic structure with macroscopic catalytic performance.

1. Introduction

Hydrogen, a clean resource possessing high energy density, has been intensely studied as one of the most valuable alternatives to fossil fuels [1,2]. To produce this resource, a promising way is to perform water splitting with auxiliary electrocatalyst [3]. To our knowledge, Pt-group metals are the most active and stable catalysts for hydrogen evolution reaction (HER) [4–6]. However, the prize would limit its scale-up application [7,8]. Thus, efforts have been focused on pursuing alternative catalysts with comparable performance.

Among the candidates, molybdenum carbide (Mo_xC), a representative member of transition-metal carbides, has been believed as one of most promising HER electrocatalysts because of its similar d-band electronic structure to the Pt-group metals [9–12]. To expose more active sites, the molybdenum carbide electrocatalysts are usually designed with various well-defined nanostructures, such as one-dimensional (1D) nanotubes [13] or 2D $\text{Mo}_2\text{C}/\text{C}$ hierarchical nanosheets [14]. However, the HER activity is intrinsically limited by the chemical properties of the molybdenum carbide. The molybdenum carbide can naturally exist in a wide range of phases presenting different properties

[15]. The flexibility in chemical/structural properties may offer insights in achieving targeting properties based on tuning the chemical components. Specifically, different crystal structures [16–18] possess different surface Mo to C ratios, leading to various catalytic properties. For instance, $\beta\text{-Mo}_2\text{C}$ exhibits a strong hydrogen-binding energy, while the HER catalyzed by this material has the penalty from the desorption step [19,20]. On the contrary, the weak Mo-H bonds or inefficient H^* adsorption in MoC restrict its HER activity [21]. Hence, it's straightforward to assume the optimal ratio exists between these two extreme cases, and tuning the atomic structure of Mo_xC may enhance its intrinsic activity for HER. In the very limited reports, increasing calcination temperature is an effective strategy for molybdenum carbide heterostructures [22–24]. However, it may lead to excess growth of the molybdenum carbides crystallites or structure collapse of the catalysts [25], reducing the density of active sites, which in turn deteriorating HER performance. Therefore, to combine these two merits, a higher intrinsic activity and more active sites, a smart design of experimental conditions is required to simultaneous optimization of the heterostructure and the nanostructure.

Herein, employing the SiO_2 as a template, a monodisperse inverse

* Corresponding authors at: School of Materials Science and Engineering, Central South University, Changsha, 410083, China.

** Corresponding author.

E-mail addresses: zwu2012@csu.edu.cn (Z. Wu), zhen.cao@kaust.edu.sa (Z. Cao), dzwang@csu.edu.cn (D. Wang).

opal structure was obtained to maximize the exposed active sites. More importantly, a novel α -MoC_{1-x}/ β -Mo₂C heterostructure can be constructed due to the confining effect of SiO₂, which can significantly enhance the intrinsic activity. As a result, by adjusting the amount of SiO₂ spheres, we have successfully adjusted the chemical/phase compositions of the Mo_xC spherical heterostructures, and an optimal composition of Mo_xC-0.4 (α -MoC_{1-x}: β -Mo₂C = 0.56/0.44) was obtained, which exhibits an excellent HER performance with a low Tafel slope of 48 mV dec⁻¹ and a good durability as 30 h in 0.5 M H₂SO₄. Furthermore, to understand the synergistic interaction between α -MoC_{1-x} and β -Mo₂C, density functional theory (DFT) was applied to investigate the H* absorption free energy for HER. And the calculations indicated that hydrogen-binding energy (ΔG_{H^*}) decreased with the decreased ratio of α -MoC_{1-x}/ β -Mo₂C, and the Mo_xC-0.4 presents the most similar ΔG_{H^*} to the platinum surface.

2. Experimental section

2.1. Materials

All chemical reagents used in this work were of analytical grade and used without further purification. Dopamine hydrochloride (C₈H₁₁O₂N·HCl), ammonium molybdate tetrahydrate (NH₄)₆Mo₇O₂₄·4H₂O) and tetraethyl orthosilicate (TEOS) were purchased from Aladdin. Pt/C (20 wt. % Pt on Vulcan XC-72R) was purchased from the Johnson Matthey Company. Nafion solution (5 wt. %) was purchased from DuPont Company (USA). All solutions were prepared using deionized water.

2.2. Synthesis of SiO₂ spheres

The SiO₂ spheres were synthesized by using a modified procedure originally described by Stöber et al. [26]. First, 17.2 mL H₂O, 2.48 mL NH₃·H₂O (25–28 wt %) and 92 mL ethanol were blended for 10 min, and then 3.44 mL TEOS was added dropwise into the above solution with magnetic stirring. After being continuously stirred at room temperature for 4 h, the clear solution became milk white and opaque. Finally, the SiO₂ spheres were collected by centrifugation after being washed with water and ethanol for several times before dried in an oven at 60 °C overnight.

2.3. Synthesis of Mo_xC

The synthesis of Mo_xC follows a self-assembled polymerization route [27–29]. Briefly, 1.2 g ammonium molybdate tetrahydrate ((NH₄)₆Mo₇O₂₄·4H₂O) was dissolved into 20 mL deionized water under stirring at room temperature for 5 min. Then, a certain amount of as-prepared SiO₂ was added into the above solution, after ultrasonic for 30 min, a uniform suspension was achieved. Subsequently, 0.4 g dopamine hydrochloride was added into the suspension, the solution quickly became brick-red. Then 40 mL of ethanol was poured into the above solution. After stirring another 5 min, the solution pH was adjusted to 8.5–9 by quickly injecting 0.4 mL NH₃·H₂O (25–28 wt %) into the above suspension. Then the mixture was stirred for 2 h and the orange-red precipitate was collected by centrifugation after repetitively washed with deionized water and absolute ethanol. Finally, the orange-red precursors were heated to 800 °C for 3 h under an argon atmosphere with a temperature ramping rate of 5 °C min⁻¹ after dried at 80 °C for 10 h. Finally, the resulted samples were leached in HF acid (20%) for 30 min to completely remove the SiO₂ spheres. The as-prepared catalysts are denoted as Mo_xC-0, Mo_xC-0.2, Mo_xC-0.4, and Mo_xC-0.8, where 0, 0.2, 0.4 and 0.8 stand for the mass of the added SiO₂ spheres (0, 0.2 g, 0.4 g and 0.8 g) in the precursor, respectively.

2.4. Preparation of working electrodes

In a typical procedure, 3 mg of catalyst and 80 μ L Nafion solution (5 wt. %) in 1 mL mixture solution of 200 μ L absolute ethanol and 800 μ L distilled water by at least 30 min sonication to form a homogeneous slurry. Afterwards, five microliters of the slurry were drop-cast onto the surface of a smooth glassy carbon electrode (GCE, diameter of 3 mm) with a catalyst loading of 213 μ g cm⁻². Finally, the modified GCE was naturally dried at room temperature and retained for use.

2.5. Physical measurements

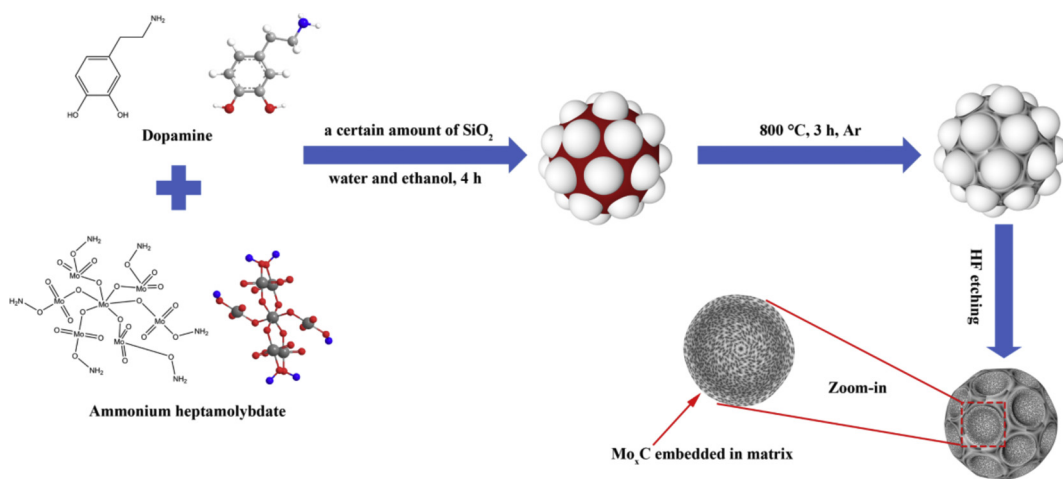
The XRD patterns were collected on a Mini Flex 600 system from 15° to 80° using a Cu K α radiation (λ = 0.154 nm). The transmission electron microscopy (TEM) and the scanning electron microscopy (SEM) images were taken on a Tecnai G² F20 transmission electron microscope and a FEI Sirion 200 scanning electron microscope, respectively. The X-ray photoelectron spectroscopy (XPS) was processed on the ESCALAB 250Xi with a monochromatic Al K α source, using the C 1 s = 284.8 eV to calibrate the binding energy value of each element. The specific surface areas and the pore width distribution were calculated by nitrogen adsorption – desorption isotherms using the Brunauer-Emmett-Teller (BET) method and the Barrett-Joyner-Halenda method, respectively, and all the samples were dried at 100 °C under vacuum over 16 h before the experiment. Raman spectra were recorded on the instrument LabRAMHR-800 of French company HRIBA with an excitation laser wavelength of 632.81 nm. ICP-OES/MS and EA were performed on the PerkinElmer Optima 5300 DV and the vario EL III, respectively. The DFT calculations were performed using the KAUST super computer.

2.6. Electrochemical measurements

All the electrochemical measurements were operated with a CHI 660E electrochemical workstation using a standard three-electrode system at room temperature. An Hg/Hg₂Cl₂ electrode (SCE, saturated KCl aqueous solution), a carbon rod and the glassy carbon electrode modified with catalysts were used as the reference electrode and the counter electrode, the work electrode, respectively. The linear sweep voltammetry (LSV) was conducted by sweeping the potential from 0.1 V to -0.4 V with a potential scan rate of 2 mV s⁻¹ in 0.5 M H₂SO₄. The electrochemical impedance spectroscopy (EIS) was performed with an amplitude of 5 mV and a frequency range from 10⁶ Hz to 1 Hz at a specific overpotential of -200 mV. The long-term cycling test was conducted by repeating up to 5000 cyclic voltammetry (CV) cycles at the potential between 0.1 and -0.4 V vs RHE with a scan rate of 50 mV s⁻¹. Additionally, current-time response was monitored for 30 h at an overpotential corresponding to a current density of -20 mA cm⁻². In this work, all the reported potentials are referenced to reversible hydrogen electrode (RHE) though the equation ($E_{vs\ RHE} = E_{vs\ SCE} + E_{o\ SCE} + 0.059\text{ pH}$) without IR corrections. All the reported current densities are calculated in terms of the geometrical surface area of the working electrode.

2.7. Simulation setup

The binding energy of the hydrogen on MoC_x surface with different Mo/C ratios was calculated at the revised Perdew-Burke-Ernzerhof (rPBE) level of density functional theory (DFT) using the VASP package [30,31]. The electrons were described using the projector augmented wave (PAW) method [32], and the energy cutoff was chosen to be 400 eV. The Brillouin zone sampling was performed using $3 \times 4 \times 1$ k-points. We constructed the model based on the α -MoC_{1-x}. Following the previous calculation scheme [25], the different Mo/C ratio was described by generating the C defects at the Mo-C slab. The binding energy of the hydrogen atoms was calculated within the computational



Scheme 1. Schematic view of the synthesis process for Mo_xC .

hydrogen electrode (CHE) framework developed in the Nørskov's group [33].

3. Results and discussion

3.1. Catalyst synthesis and characterization

The monodisperse inverse opal-like Mo_xC catalysts were prepared as schematically illustrated in **Scheme 1**. The Mo_xC catalysts were obtained from the assembly of dopamine-HCl, ammonium heptamolybdate (AHM) and SiO_2 . During the polymerization of Mo-dopamine, the SiO_2 was enshrouded in and outside of the Mo-polydopamine (Mo-PDA) spheres. After being dried, this catalyst was subjected to carbonization. Then, the inverse opal-like structure was achieved after HF etching. The as-prepared catalysts are denoted as $\text{Mo}_x\text{C-0}$, $\text{Mo}_x\text{C-0.2}$, $\text{Mo}_x\text{C-0.4}$, and $\text{Mo}_x\text{C-0.8}$, where 0, 0.2, 0.4 and 0.8 stand for the mass of

the added SiO_2 spheres (0, 0.2 g, 0.4 g and 0.8 g) in the precursor, respectively. As shown in **Fig. 1a**, the phases of the Mo_xC catalysts were confirmed by the X-ray diffraction (XRD). The $\text{Mo}_x\text{C-0}$ sample shows characteristic diffraction peaks at approximately 36.7° , 42.3° , 62.0° and 74.6° , corresponding to (111), (200), (220) and (311) facets of the pure $\alpha\text{-MoC}_{1-x}$ phase (JCPDS no. 89-2868), which are consistent with previous reports [24,34]. It's worth noting that one new peak at 39.4° can be found in the XRD patterns of the $\text{Mo}_x\text{C-0.2}$ samples, which should be ascribed to the generation of $\beta\text{-Mo}_2\text{C}$ due to the addition of SiO_2 . Moreover, by increasing the feeding content of SiO_2 , more other diffraction peaks at 34.4° , 38.0° , 52.1° , 61.6° , 69.5° , 74.6° and 75.5° in the XRD patterns of the $\text{Mo}_x\text{C-0.4}$ and $\text{Mo}_x\text{C-0.8}$ can be found, further demonstrating the existence of the $\beta\text{-Mo}_2\text{C}$ phase (JCPDS no. 35-0787). More addition of SiO_2 leads to more and sharper diffraction peaks, indicating a higher yield of $\beta\text{-Mo}_2\text{C}$. Hence, it can be concluded that the template of SiO_2 can trigger the phase transformation from $\alpha\text{-MoC}_{1-x}$ to

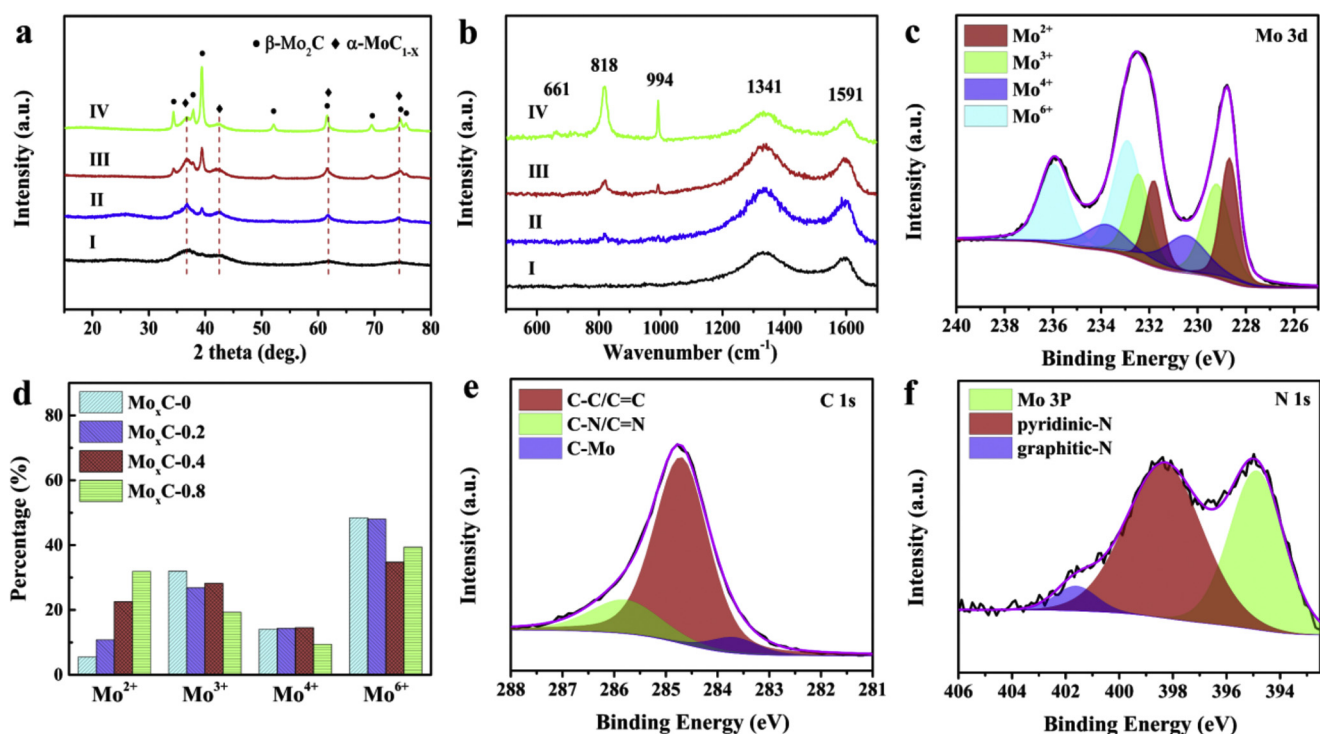


Fig. 1. (a) The XRD patterns and (b) Raman spectra of the as-prepared Mo_xC catalysts (I: $\text{Mo}_x\text{C-0}$, II: $\text{Mo}_x\text{C-0.2}$, III: $\text{Mo}_x\text{C-0.4}$, IV: $\text{Mo}_x\text{C-0.8}$). (c) Mo 3d of the $\text{Mo}_x\text{C-0.4}$, (d) compositions of various Mo species of the as-prepared Mo_xC catalysts, (e) C 1s, and (f) N 1s of the $\text{Mo}_x\text{C-0.4}$.

β -Mo₂C, resulting in a heterostructure of α -MoC_{1-x}/ β -Mo₂C with a suitable content. To understand the formation of the Mo_xC heterostructures, the sectional view of the SiO₂@Mo-PDA are shown in Fig. S1. Due the confining effect of SiO₂, the adjacent two SiO₂ spheres frame the thin area a, while the area b stacked by multiple SiO₂ spheres belongs to the thick area. During the calcination process, the residual carbon in thick area b makes it become the carbon-rich area which favors the formation of α -MoC_{1-x}, whereas the thin area a results in the relatively carbon-poor area, which may lead to the formation of β -Mo₂C [35,36]. When increasing the amount of SiO₂, the SiO₂ would be arranged more tightly, which would bring about more thin area for the generation of β -Mo₂C. Thus, it is possible to construct a α -MoC_{1-x}/ β -Mo₂C heterostructure by adjusting the amount of SiO₂.

The Mo_xC catalysts were further characterized by Raman spectroscopy. As shown in Fig. 1b, all the Mo_xC samples exhibit two pronounced vibration peaks at around 1341 and 1591 cm⁻¹, which are assigned to the D and G bands of amorphous carbon relevant to the defective carbon and the sp²-hybridized graphitic carbon, respectively [37]. The intensity ratios of D to G bands range from 1.5 to 1.8 evidence that the carbon component is disordered with many defects. Apart from the carbon peaks, there are several other peaks at 662, 817, and 992 cm⁻¹, which is consistent with the formation of β -Mo₂C [38,39]. Similar to the XRD result, the intensities of these peaks are enhanced with the increment of SiO₂.

The surface electronic state and chemical composition of the Mo_xC-0.4, as a representative sample, were characterized using the X-ray photoelectron spectroscopy (XPS). As shown in Fig. 1c, the Mo 3d XPS spectrum can be fitted using four deconvoluted doublets. Among them, the two doublets at 230.6 eV, 233.8 eV and 232.8 eV, 236.0 eV corresponding to Mo⁴⁺ and Mo⁶⁺ are associated with the inactive MoO₂ and MoO₃, which can be attributed to the inevitably surface oxidation through air contact [35,40]. The peaks located at 228.6 eV and 231.8 eV are assigned to Mo²⁺ 3d_{5/2} and 3d_{3/2}, respectively, consistent with the presence of β -Mo₂C phase [27]. Furthermore, another doublet at 229.2 eV and 232.5 eV (Mo³⁺ 3d_{5/2} and 3d_{3/2}) can be ascribed to the Mo-C bond in α -MoC_{1-x} phase [20,41]. The detailed compositions of the Mo valence states for the as-obtained Mo_xC are further summarized in Fig. 1d, Tables S1 and S2. The Mo⁴⁺ and Mo⁶⁺ species barely contribute to HER activities [20,42], and more attention is paid on the active species, including Mo²⁺ and Mo³⁺. The Mo²⁺ and Mo³⁺ contents in the Mo_xC-0 are found to be 5.53 at. % and 31.96 at. %, respectively, while those in the Mo_xC-0.8 are 31.90 at. % and 19.3 at. %, indicating that the predominant α -MoC_{1-x} is transformed to β -Mo₂C in the as-prepared Mo_xC. Besides, the mole ratios of Mo²⁺/Mo³⁺ increases with the increment of SiO₂ feeding mass, which is also observed in the XRD. The XPS spectrum of C 1s in Fig. 1e can be deconvoluted into three peaks: the peak at 283.7 eV relates to the C–Mo bond, whereas the peak at 284.7 eV results from the C–C/C=C bond [43]. The peak at 285.8 eV, however, can be ascribed to a C–N/C=N bond, indicating the existence of N atoms in the Mo_xC samples [44]. In Fig. 1f, the N 1s signal of the Mo_xC, derived from the N element in the Mo-PDA precursors, can be fitted using three peaks located at binding energies of 394.8 eV, 398.3 eV and 401.7 eV matching with Mo 3p, pyridinic N and graphitic N, respectively [45,46], which indicates that the N is doped into the carbon support [47,48].

The morphology and structure of the Mo_xC-0.4 were further investigated by scanning electron microscopy (SEM) and transmission electron microscopy (TEM). As observed in Fig. 2b and c, the Mo_xC-0.4 catalysts are consisted of monodisperse spheres with diameters around 0.5–1.5 μ m, and each microsphere exhibits an inverse opal-like structure with a pore size of approximately 200 nm, which is consistent with SiO₂ templates (Fig. 2a). Besides, the morphology of the Mo_xC-0, Mo_xC-0.2 and Mo_xC-0.6 are also verified through the SEM investigation (Fig. S3). In absence of SiO₂, only sphere-like Mo_xC with relatively smooth surfaces are yielded. When the mass of SiO₂ is fixed at 0.2 g, pore-structure is rarely observed in the Mo_xC spheres. However, increasing

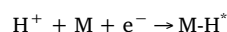
the mass of SiO₂ to 0.8 g, the overall sizes and morphology are analogue to the Mo_xC-0.4. The microporous structure and pore size can also be confirmed by TEM (Fig. 2d). Intriguingly, as depicted in Fig. 2e and f, numerous Mo_xC nanocrystals are uniformly embedded in the continuous interconnecting carbonaceous matrix. Besides, high-resolution TEM images (Fig. 2g and h) indicate that the lattice spacing of nanocrystal is estimated to be \sim 0.261 nm, 0.237 nm, 0.228 nm, corresponding to the (100), (002) and (101) facets of β -Mo₂C, respectively. Noticeably, the (111) lattice fringes of α -MoC_{1-x} are also identified in Fig. 2g. This result is in good agreement with the XRD information. Besides, the Brunauer-Emmett-Teller (BET) specific surface areas and the corresponding Barrett-Joyner-Halenda (BJH) pore-size distribution of the Mo_xC-0 and Mo_xC-0.4 were also revealed by the nitrogen adsorption/desorption isotherm linear plot (Fig. S4). The Mo_xC-0.4 shows a larger BET surface area of 60.4 m² g⁻¹ and a bigger average pore size of 14.3 nm than those of Mo_xC-0 (20.4 m² g⁻¹, 8.4 nm), demonstrating that the inverse opal-like structure can significantly increase exposed surface area.

3.2. Electrocatalytic HER performance

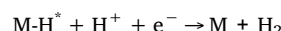
The HER activities of the as-prepared Mo_xC catalysts were investigated in an acidic electrolyte by the linear sweep voltammetry (LSV). Fig. 3a displays their polarization curves at a scan rate of 2 mV s⁻¹ in 0.5 M H₂SO₄. As a reference, the commercially available benchmark Pt/C catalyst (20 wt %, Johnson Matthey) with the same mass loading of 213 μ g cm⁻² was also measured, exhibiting a good catalytic activity with an approximately zero onset overpotential (η_1 , $j = -1$ mA cm⁻²), which is consistent with the previous study [49–51]. Among the Mo_xC catalysts, the Mo_xC-0.4 with a suitable ratio of α -MoC_{1-x} and β -Mo₂C (0.56/0.44) exhibits the highest HER activity with an over potential of -155 mV to achieve a current density (j) of -10 mA cm⁻², which is obviously lower than those of Mo_xC-0 (α -MoC_{1-x}/ β -Mo₂C = 0.85/0.15, -310 mV), Mo_xC-0.2 (α -MoC_{1-x}/ β -Mo₂C = 0.71/0.29, -285 mV) and Mo_xC-0.8 (α -MoC_{1-x}/ β -Mo₂C = 0.38/0.62, -190 mV). Notably, this performance is comparable or superior to those well-known Mo_xC-based electrocatalysts as summarized in Fig. 3c (Table S5). The HER performance of the synthesized Mo_xC is enhanced with increased percentage of β -Mo₂C phase initially, peaks at the Mo_xC-0.4 and then descends owing to the decreased content of α -MoC_{1-x}.

To better understand the HER activity from a kinetic viewpoint, the Tafel slopes were obtained from the corresponding LSV curves through the Tafel equation ($\eta = b \log j + a$, where b and j are the Tafel slope and the current density, respectively). Normally, a smaller Tafel slope indicates a lower overpotential when increasing the same current density, indicating a more efficient HER catalyst [52,53]. The Mo_xC-0.4 exhibits a remarkably smaller Tafel slope of 48 mV dec⁻¹, indicating a fast increase of hydrogen generation rate compared with the other three catalysts. Ordinarily, it is accepted that the HER occurring on the surface of electrodes involves two steps in acid media. The first one is the electrochemical adsorption of hydrogen (Volmer reaction), whereas the second step is the desorption of adsorbed hydrogen, including the electrochemical desorption (Heyrovsky reaction) or the chemical desorption (Tafel reaction). The accepted reaction mechanisms are shown here:

(1) electrochemical adsorption of hydrogen (Volmer reaction)



(2) electrochemical desorption (Heyrovsky reaction)



(3) chemical desorption (Tafel reaction)

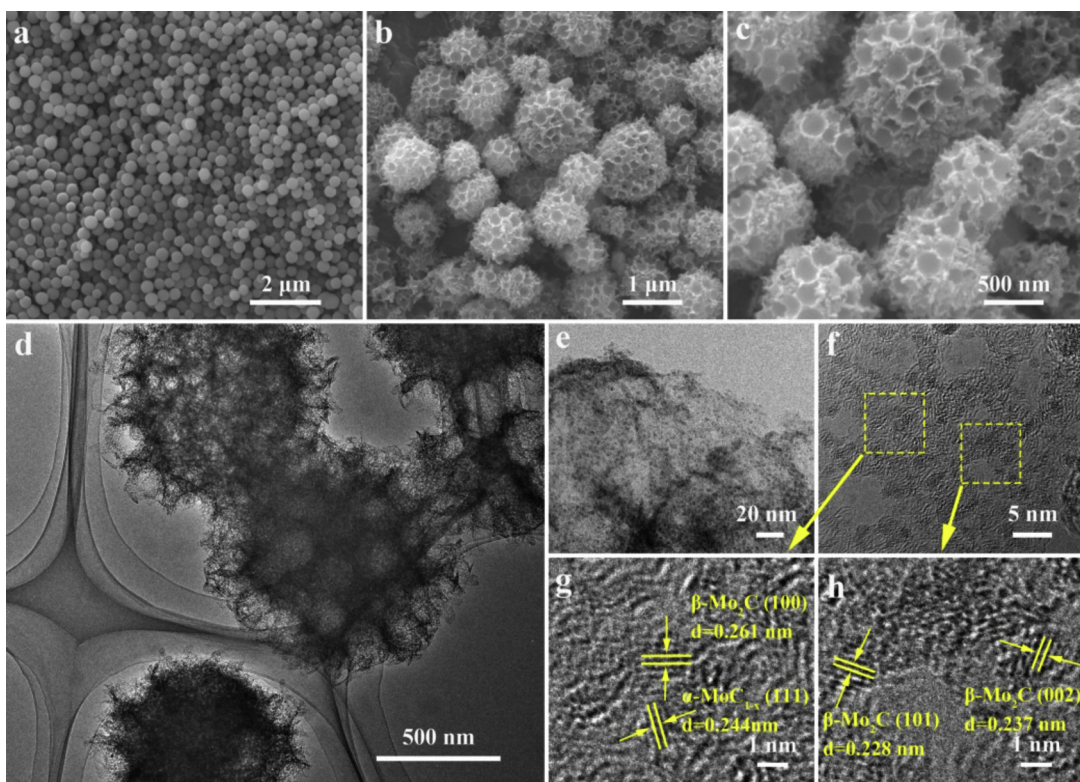
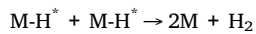


Fig. 2. (a) SEM image of the SiO₂ template, (b, c) SEM images, (d, e) TEM images and (f) HRTEM image of the Mo_xC-0.4, and (g, h) images of the region enclosed by the yellow square of (f). (For interpretation of the references to colour in this figure legend, the reader is referred to the web version of this article).



The Tafel slope depends on the rate-determining step in the process of hydrogen evolution reaction. Normally, a Tafel slope of 120 mV

dec⁻¹ implies that the Volmer reaction is the rate-determining step, whereas Tafel slopes of 30 and 40 mV dec⁻¹ intimate the Tafel and Heyrovsky reactions, respectively [54–56]. Given that the Tafel reaction as the rate-determining step for only a few noble metals, the Tafel slope from 48 to 79 mV dec⁻¹ over the Mo_xC catalysts denote that the

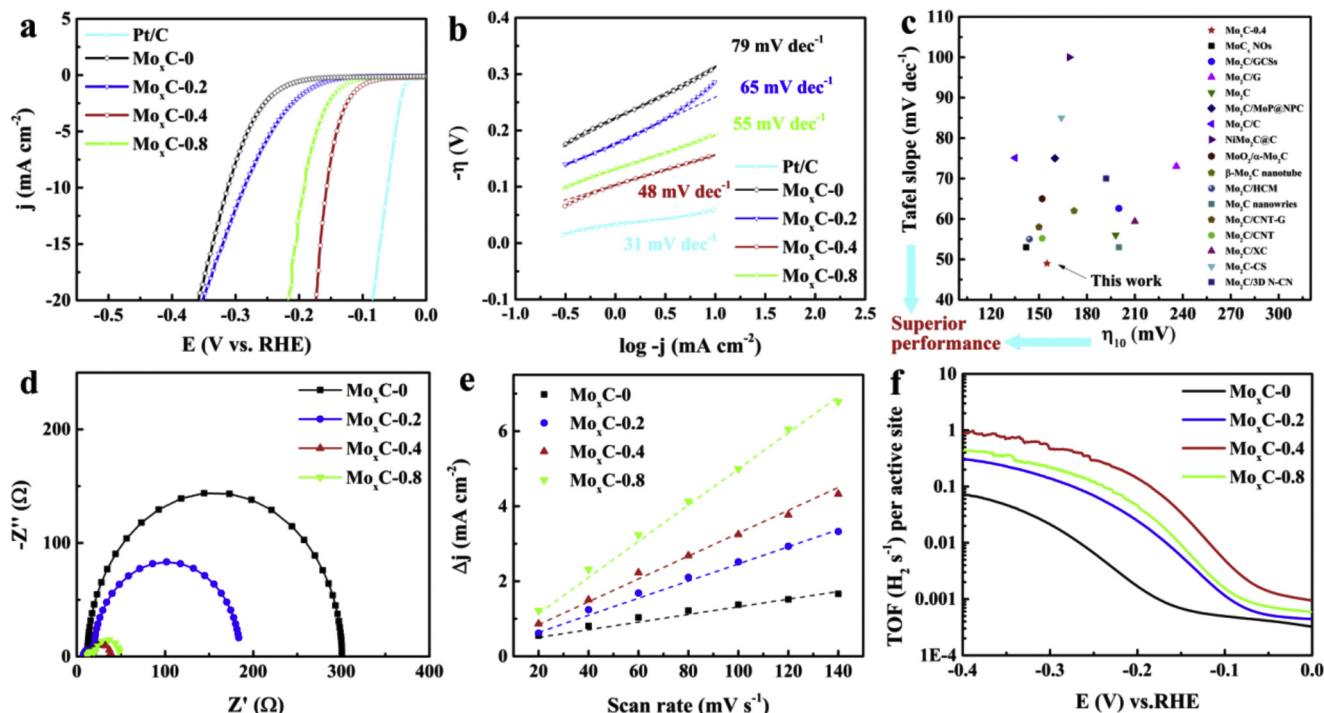


Fig. 3. (a) Polarization curves, and (b) Tafel slopes of the Mo_xC catalysts, (c) Comparison of the Tafel slope and η_{10} of Mo_xC-0.4 with other Mo_xC-based electrocatalysts, (d) Nyquist plots, (e) Measured capacitive currents plotted as a function of scan rate, and (f) TOF values of the Mo_xC catalysts.

HER mechanism belongs to the mixed Volmer–Heyrovsky mechanism and the Heyrovsky reaction acts as the rate-determining step. Besides, the exchange current densities (j_0) of the as-prepared Mo_xC catalysts were also further calculated by extrapolating the Tafel plots. And the $\text{Mo}_x\text{C}-0.4$ possesses a larger exchange current density (j_0) of $9.1 \mu\text{A cm}^{-2}$ than those of $\text{Mo}_x\text{C}-0$ ($1.6 \mu\text{A cm}^{-2}$), $\text{Mo}_x\text{C}-0.2$ ($2.0 \mu\text{A cm}^{-2}$) and $\text{Mo}_x\text{C}-0.8$ ($4.3 \mu\text{A cm}^{-2}$), demonstrating a higher inherent HER activity of the $\text{Mo}_x\text{C}-0.4$ catalyst.

Electrochemical impedance spectroscopy (EIS) measurements were also performed to provide insights in electrode kinetics during the HER process. The Nyquist plots were fitted using the equivalent circuits in Fig. S5 (Fig.S5a for Mo_xC and Fig.S5b for $\text{Mo}_x\text{C}-0.2$, $\text{Mo}_x\text{C}-0.4$, and $\text{Mo}_x\text{C}-0.8$). For $\text{Mo}_x\text{C}-0.2$, $\text{Mo}_x\text{C}-0.4$, and $\text{Mo}_x\text{C}-0.8$, the first semicircle at high frequencies corresponds to the surface porosity (R_p) and the second is related to the charge transfer resistance (R_{ct}) of H^+ reaction at the interface between electrode-electrolyte. While for $\text{Mo}_x\text{C}-0$, the only semicircle is also related to the charge transfer (R_{ct}) process. More detailed resistance values are listed in Table S6. The calculated R_{ct} values of $\text{Mo}_x\text{C}-0.4$ (20.9Ω) is smaller than the $\text{Mo}_x\text{C}-0$ (288.5Ω), $\text{Mo}_x\text{C}-0.2$ (166.5Ω) and $\text{Mo}_x\text{C}-0.8$ (28.8Ω), suggesting a faster Faradaic process and superior HER kinetics [57].

The electrochemically active surface area (ECSA) of the Mo_xC catalysts was calculated by measuring the double-layer capacitance (C_{dl}) derived from the cyclic voltammetry (CV) measurements at different scan rates (Table 1 and Fig. S6). The measured current density plotted as a function of scan rate to extract the C_{dl} value, which is equivalent to the half of the slope value in Fig. 3e. One can see that the $\text{Mo}_x\text{C}-0.4$ exhibits an ECSA value of 355.25 cm^2 ECSA, about 3 times larger than that of the $\text{Mo}_x\text{C}-0$ (113.88 cm^2 ECSA). As expected, the ECSA value is increased with increasing the adding amount of SiO_2 , suggesting that inverse opal-like structure of the Mo_xC can increase the active electrocatalytic area and expose more active sites for HER. The turnover frequency (TOF) is another useful parameter to evaluate the intrinsic activities of catalysts. The related reckonings of TOF are recorded in the Supporting Information. Excitingly, the TOF of the $\text{Mo}_x\text{C}-0.4$ is found to be the highest among the as-prepared Mo_xC catalysts, which gives a solid evidence for the synergic enhancement between $\alpha\text{-MoC}_{1-x}$ and $\beta\text{-Mo}_2\text{C}$. In the meantime, compared with the $\text{Mo}_x\text{C}-0.8$, the $\text{Mo}_x\text{C}-0.4$ with a smaller ECSA value and a higher TOF possesses a better HER performance, confirming that the synergistic effect between $\alpha\text{-MoC}_{1-x}$ and $\beta\text{-Mo}_2\text{C}$ dominates the HER activity of the Mo_xC catalysts.

Besides, the stability of catalysts is an important indicator for practical application. A long-term cycling measurement of the $\text{Mo}_x\text{C}-0.4$ was continuously conducted using cyclic voltammetry (CV) for 5000 cycles from 0.1 V to -0.4 V at 50 mV s^{-1} . As shown in Fig. S7a, only a slight degradation of current density is observed after scanning, indicating a good stability of $\text{Mo}_x\text{C}-0.4$. In addition, a long-time successive hydrogen production test was also performed at 20 mA cm^{-2} for 30 h (Fig. S7b). The $\text{Mo}_x\text{C}-0.4$ catalysts exhibit a high activity and stable life over long-time testing, further demonstrating the excellent stability.

3.3. Optimized hydrogen binding on Mo_xC surface

Thereafter, DFT calculations (details in Computational Methods)

Table 1
Summary of information over various Mo_xC samples.

Catalysts	Tafel slope (mV dec $^{-1}$)	j_0 ($\mu\text{A cm}^{-2}$)	η_1 (mV)	η_{10} (mV)	C_{dl} ($\mu\text{F cm}^{-2}$)	A_{ECSA} (cm 2 ECSA)	R_{ct} (Ω)
$\text{Mo}_x\text{C}-0$	79	1.6	220	310	4555	113.9	288.5
$\text{Mo}_x\text{C}-0.2$	65	2.0	175	285	11020	275.5	166.5
$\text{Mo}_x\text{C}-0.4$	48	9.1	100	155	14210	355.3	20.9
$\text{Mo}_x\text{C}-0.8$	55	4.3	130	190	23150	578.8	28.8

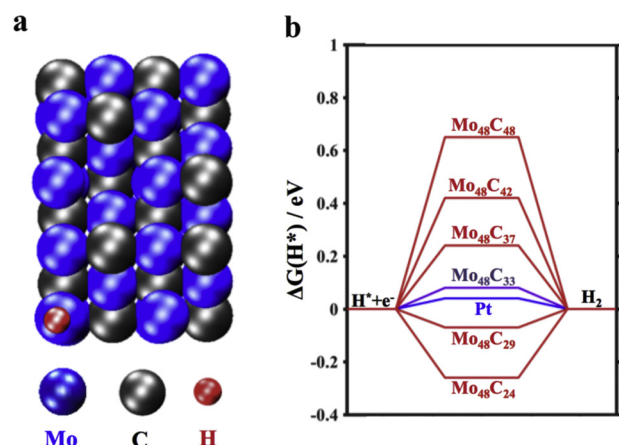


Fig. 4. DFT calculations of the binding energy of the adsorbed hydrogen on Mo_xC surface. (a) Demonstrate the atomic structure of the adsorbed hydrogen on $\text{Mo}_{48}\text{C}_{33}$ surface with the lowest energy. (b) Demonstrate the binding energy of the adsorbed hydrogen on different material surfaces.

were performed to evaluate the binding energy (ΔG_{H^*}) of the adsorbed hydrogen on Mo_xC surface (Fig. 4). We constructed models using different Mo-C ratios ranging from 1:1 to 2:1, where $\text{Mo}_{48}\text{C}_{42}$, $\text{Mo}_{48}\text{C}_{37}$, $\text{Mo}_{48}\text{C}_{33}$, and $\text{Mo}_{48}\text{C}_{29}$ correspond to $\text{Mo}_x\text{C}-0$, $\text{Mo}_x\text{C}-0.2$, $\text{Mo}_x\text{C}-0.4$ and $\text{Mo}_x\text{C}-0.8$, respectively. For each ratio, different initial positions for the hydrogen atoms were tested (Fig. S8), and the configuration with the lowest energy was chosen to calculate the hydrogen binding energy. In DFT calculations, the adsorption of H on $\text{Mo}_{48}\text{C}_{24}$ ($\beta\text{-Mo}_2\text{C}$) was found to be too strong, whereas it was too weak on $\text{Mo}_{48}\text{C}_{48}$ ($\alpha\text{-MoC}_{1-x}$). With increasing $\beta\text{-Mo}_2\text{C}$ content, the positive ΔG_{H^*} decreases close to zero, indicating the strengthening of adsorbed H. Notably, with excessive $\beta\text{-Mo}_2\text{C}$, a negative ΔG_{H^*} suggests that the adsorbed H becomes too strong, which in turn inhibits H desorption. Among the constructed models, the $\text{Mo}_{48}\text{C}_{33}$ ($\text{Mo}_x\text{C}-0.4$) presents the most similar binding energy compared with the platinum surface (0.08 vs. 0.04 eV), which is consistent with the result of the Tafel plots (Fig. 3b). Such evaluation gives a thermodynamic factor behind the HER performance of the synthesized Mo_xC .

According to above experiments and calculations, the enhanced HER performance of $\text{Mo}_x\text{C}-0.4$ is related to the following factors: (i) the special inverse opal-like Mo_xC nanospheres greatly increase the surface area and expose more active sites for HER. (ii) the appropriate composite between $\alpha\text{-MoC}_{1-x}$ and $\beta\text{-Mo}_2\text{C}$ results in a strong synergistic effect that improves the intrinsic catalytic activity, as revealed by the optimized binding energy (ΔG_{H^*}) of Mo_xC .

4. Conclusion

In summary, monodisperse inverse opal Mo_xC nanospheres have been successfully synthesized via a facile strategy using SiO_2 as templates. Moreover, due to the confining effect of SiO_2 , a novel $\alpha\text{-MoC}_{1-x}$ / $\beta\text{-Mo}_2\text{C}$ heterostructure has been constructed. The inverse opal structure possesses high BET and ECSA, significantly increasing the number of active sites. In the meantime, the $\text{Mo}_x\text{C}-0.4$ with an appropriate mole ratio of $\alpha\text{-MoC}_{1-x}$ / $\beta\text{-Mo}_2\text{C}$ (0.56/0.44) exhibits a strong synergistic effect with a high TOF value and a large exchange current densities (j_0) of $9.1 \mu\text{A cm}^{-2}$. Theoretical calculations further verify that the $\text{Mo}_x\text{C}-0.4$ possesses the most similar ΔG_{H^*} to the platinum surface. As a result, the $\text{Mo}_x\text{C}-0.4$ shows an outstanding HER activity and stability, making it a promising alternative to replace precious-metal HER catalysts. Furthermore, this work will open a new horizon for improving HER performance by rational engineering of nanostructure together with heterostructure.

Conflict of interests

The authors declare no conflict of interests.

Acknowledgements

Financial supports from the National Natural Science Foundation of China (Grants 51572301), National Key R&D Program of China (2017YFB0306000), Hunan Provincial Natural Science Foundation (Grants 2016JJ3153) and the Innovation-Driven Project of Central South University (Grants 502221802) are gratefully acknowledged. The computational simulations were performed using the KAUST super computing resources.

Appendix A. Supplementary data

Supplementary material related to this article can be found, in the online version, at doi:<https://doi.org/10.1016/j.apcatb.2019.01.086>.

References

- [1] J. Greeley, T.F. Jaramillo, J. Bonde, I.B. Chorkendorff, J.K. Nørskov, Computational High-throughput Screening of Electrocatalytic Materials for Hydrogen Evolution, *Materials for Sustainable Energy*, Co-Published with Macmillan Publishers Ltd, UK, 2010, pp. 280–284.
- [2] J.A. Turner, Sustainable hydrogen production, *Science* 305 (2004) 972–974.
- [3] M.S. Faber, S. Jin, Earth-abundant inorganic electrocatalysts and their nanostructures for energy conversion applications, *Energy Environ. Sci.* 7 (2014) 3519–3542.
- [4] D. Akyüz, B. Keskin, U. Şahintürk, A. Koca, Electrocatalytic hydrogen evolution reaction on reduced graphene oxide electrode decorated with cobaltpthalocyanine, *Appl. Catal. B-Environ.* 188 (2016) 217–226.
- [5] S. Reddy, R. Du, L. Kang, N. Mao, J. Zhang, Three dimensional CNTs aerogel/MoS_x as an electrocatalyst for hydrogen evolution reaction, *Appl. Catal. B-Environ.* 194 (2016) 16–21.
- [6] H. Lv, X. Chen, D. Xu, Y. Hu, H. Zheng, S.L. Suib, B. Liu, Ultrathin PdPt bimetallic nanowires with enhanced electrocatalytic performance for hydrogen evolution reaction, *Appl. Catal. B-Environ.* 238 (2018) 525–532.
- [7] W. Zhou, J. Jia, J. Lu, L. Yang, D. Hou, G. Li, S. Chen, Recent developments of carbon-based electrocatalysts for hydrogen evolution reaction, *Nano Energy* 28 (2016) 29–43.
- [8] J. Li, W. Hong, C. Jian, Q. Cai, W. Liu, Seamless tungsten disulfide-tungsten heterojunction with abundant exposed active sites for efficient hydrogen evolution, *Appl. Catal. B-Environ.* 244 (2019) 320–326.
- [9] W. Zheng, T.P. Cotter, P. Kaghazchi, T. Jacob, B. Frank, K. Schlichte, W. Zhang, D.S. Su, F. Schuth, R. Schlogl, Experimental and theoretical investigation of molybdenum carbide and nitride as catalysts for ammonia decomposition, *J. Am. Chem. Soc.* 135 (2013) 3458–3464.
- [10] M. Qamar, A. Adam, B. Merzougui, A. Helal, O. Abdulhamid, M.N. Siddiqui, Metal–organic framework-guided growth of Mo₂C embedded in mesoporous carbon as a high-performance and stable electrocatalyst for the hydrogen evolution reaction, *J. Mater. Chem. A* 4 (2016) 16225–16232.
- [11] S. Jing, L. Zhang, L. Luo, J. Lu, S. Yin, P.K. Shen, P. Tsakaros, N-Doped Porous Molybdenum Carbide Nanobelts as Efficient Catalysts for Hydrogen Evolution Reaction, *Appl. Catal. B-Environ.* 224 (2018) 533–540.
- [12] S.K. Kim, Y. Qiu, Y.-J. Zhang, R. Hurt, A. Peterson, Nanocomposites of transition-metal carbides on reduced graphite oxide as catalysts for the hydrogen evolution reaction, *Appl. Catal. B-Environ.* 235 (2018) 36–44.
- [13] F.X. Ma, H.B. Wu, B.Y. Xia, C.Y. Xu, X.W. Lou, Hierarchical beta-Mo₂C Nanotubes Organized by Ultrathin Nanosheets as a Highly Efficient Electrocatalyst for Hydrogen Production, *Angew. Chem. Int. Ed. Engl.* 54 (2015) 15395–15399.
- [14] C. Wu, J. Li, Unique Hierarchical Mo₂C/C Nanosheet Hybrids as Active Electrocatalyst for Hydrogen Evolution Reaction, *ACS Appl. Mater. Interfaces* 9 (2017) 41314–41322.
- [15] Y. Zhong, X. Xia, F. Shi, J. Zhan, J. Tu, H.J. Fan, Transition metal carbides and nitrides in energy storage and conversion, *Adv. Sci.* 3 (2016) 1500286.
- [16] C. Wan, Y.N. Regmi, B.M. Leonard, Multiple phases of molybdenum carbide as electrocatalysts for the hydrogen evolution reaction, *Angew. Chem. Int. Ed. Engl.* 53 (2014) 6407–6410.
- [17] R. Marchand, X. Gouin, F. Tessier, Y. Laurent, New routes to molybdenum nitrides and oxynitrides: preparation and characterization of new phases, in: S.T. Oyama (Ed.), *The Chemistry of Transition Metal Carbides and Nitrides*, Springer, Netherlands, Dordrecht, 1996, pp. 252–273.
- [18] H.W. Hugosson, O. Eriksson, L. Nordström, U. Jansson, L. Fast, A. Delin, J.M. Wills, B. Johansson, Theory of phase stabilities and bonding mechanisms in stoichiometric and substoichiometric molybdenum carbide, *J. Appl. Phys.* 86 (1999) 3758–3767.
- [19] R. Michalsky, Y.-J. Zhang, A.A. Peterson, Trends in the hydrogen evolution activity of metal carbide catalysts, *ACS Catal.* 4 (2014) 1274–1278.
- [20] H. Lin, Z. Shi, S. He, X. Yu, S. Wang, Q. Gao, Y. Tang, Heteronanowires of MoC–Mo₂C as efficient electrocatalysts for hydrogen evolution reaction, *Chem. Sci.* 7 (2016) 3399–3405.
- [21] C. He, J. Tao, Synthesis of nanostructured clean surface molybdenum carbides on graphene sheets as efficient and stable hydrogen evolution reaction catalysts, *Chem. Commun.* 51 (2015) 8323–8325.
- [22] J. Dong, Q. Wu, C.P. Huang, W.F. Yao, Q.J. Xu, Cost effective Mo rich Mo₂C electrocatalysts for the hydrogen evolution reaction, *J. Mater. Chem. A* 6 (2018) 10028–10035.
- [23] C. Lv, Z. Huang, Q. Yang, C. Zhang, Nanocomposite of MoO₃ and MoC loaded on porous carbon as an efficient electrocatalyst for hydrogen evolution reaction, *Inorg. Chem. Front.* 5 (2018) 446–453.
- [24] J. Gao, Y. Wu, C. Jia, Z. Zhong, F. Gao, Y. Yang, B. Liu, Controllable synthesis of α -MoC_{1-x} and β -Mo₂C nanowires for highly selective CO₂ reduction to CO, *Catal. Commun.* 84 (2016) 147–150.
- [25] F. Li, X. Zhao, J. Mahmood, M.S. Okyay, S.M. Jung, I. Ahmad, S.J. Kim, G.F. Han, N. Park, J.B. Baek, Macroporous Inverse Opal-like Mo_xC with Incorporated Mo Vacancies for Significantly Enhanced Hydrogen Evolution, *ACS Nano* 11 (2017) 7527–7533.
- [26] W. Stöber, A. Fink, E. Bohn, Controlled growth of monodisperse silica spheres in the micron size range, *J. Colloid Interface Sci.* 26 (1968) 62–69.
- [27] Y. Huang, Q. Gong, X. Song, K. Feng, K. Nie, F. Zhao, Y. Wang, M. Zeng, J. Zhong, Y. Li, Mo₂C nanoparticles dispersed on hierarchical carbon microflowers for efficient electrocatalytic hydrogen evolution, *ACS Nano* 10 (2016) 11337–11343.
- [28] J. Chen, Y. Huang, F. Zhao, H. Ye, Y. Wang, J. Zhou, Y. Liu, Y. Li, A hierarchical α -MoC_{1-x} hybrid nanostructure for lithium-ion storage, *J. Mater. Chem. A* 5 (2017) 8125–8132.
- [29] C. Wang, L. Sun, F. Zhang, X. Wang, Q. Sun, Y. Cheng, L. Wang, Formation of Mo-Polydopamine hollow spheres and their conversions to MoO₂/C and Mo₂C/C for efficient electrochemical energy storage and catalyst, *Small* 13 (2017).
- [30] G. Kresse, J. Furthmüller, Efficient iterative schemes for ab initio total-energy calculations using a plane-wave basis set, *Phys. Rev. B* 54 (1996) 11169–11186.
- [31] B. Hammer, L.B. Hansen, J.K. Nørskov, Improved adsorption energetics within density-functional theory using revised Perdew-Burke-Ernzerhof functionals, *Phys. Rev. B* 59 (1999) 7413–7421.
- [32] G. Kresse, D. Joubert, From ultrasoft pseudopotentials to the projector augmented-wave method, *Phys. Rev. B* 59 (1999) 1758–1775.
- [33] A.A. Peterson, F. Abild-Pedersen, F. Studt, J. Rossmeisl, J.K. Nørskov, How copper catalyzes the electroreduction of carbon dioxide into hydrocarbon fuels, *Energy Environ. Sci.* 3 (2010) 1311–1315.
- [34] F.G. Baddour, C.P. Nash, J.A. Schaidle, D.A. Ruddy, Synthesis of alpha-MoC_{1-x} nanoparticles with a surface-modified SBA-15 hard template: determination of structure-function relationships in acetic acid deoxygenation, *Angew. Chem. Int. Ed. Engl.* 55 (2016) 9026–9029.
- [35] L. Ji, J. Wang, L. Guo, Z. Chen, In situ O₂-emission assisted synthesis of molybdenum carbide nanomaterials as an efficient electrocatalyst for hydrogen production in both acidic and alkaline media, *J. Mater. Chem. A* 5 (2017) 5178–5186.
- [36] C. Wan, N.A. Knight, B.M. Leonard, Crystal structure and morphology control of molybdenum carbide nanomaterials synthesized from an amine–metal oxide composite, *Chem. Commun.* 49 (2013) 10409–10411.
- [37] L.F. Pan, Y.H. Li, S. Yang, P.F. Liu, M.Q. Yu, H.G. Yang, Molybdenum carbide stabilized on graphene with high electrocatalytic activity for hydrogen evolution reaction, *Chem. Commun.* 50 (2014) 13135–13137.
- [38] T.C. Xiao, A.P.E. York, H. Al-Megren, C.V. Williams, H.T. Wang, M.L.H. Green, Preparation and characterisation of bimetallic cobalt and molybdenum carbides, *J. Catal.* 202 (2001) 100–109.
- [39] M.-L. Frauwallner, F. López-Linares, J. Lara-Romero, C.E. Scott, V. Ali, E. Hernández, P. Pereira-Almao, Toluene hydrogenation at low temperature using a molybdenum carbide catalyst, *Appl. Catal. A: Gen.* 394 (2011) 62–70.
- [40] W. Cui, N. Cheng, Q. Liu, C. Ge, A.M. Asiri, X. Sun, Mo₂C nanoparticles decorated graphitic carbon sheets: biopolymer-derived solid-state synthesis and application as an efficient electrocatalyst for hydrogen generation, *ACS Catal.* 4 (2014) 2658–2661.
- [41] Z. Cheng, J. Gao, Q. Fu, C. Li, X. Wang, Y. Xiao, Y. Zhao, Z. Zhang, L. Qu, Interconnected molybdenum carbide-based nanoribbons for highly efficient and ultrastable hydrogen evolution, *ACS Appl. Mater. Interfaces* 9 (2017) 24608–24615.
- [42] J. Xiong, J. Li, J. Shi, X. Zhang, N.T. Suen, Z. Liu, Y. Huang, G. Xu, W. Cai, X. Lei, L. Feng, Z. Yang, L. Huang, H. Cheng, In situ engineering of double-phase interface in Mo/Mo₂C heteronanosheets for boosted hydrogen evolution reaction, *ACS Energy Lett.* 3 (2018) 341–348.
- [43] W. Zhang, H. Huang, F. Li, K. Deng, X. Wang, Palladium nanoparticles supported on graphitic carbon nitride-modified reduced graphene oxide as highly efficient catalysts for formic acid and methanol electrooxidation, *J. Mater. Chem. A* 2 (2014) 19084–19094.
- [44] Q. Hu, X. Liu, B. Zhu, L. Fan, X. Chai, Q. Zhang, J. Liu, C. He, Z. Lin, Crafting MoC₂-doped bimetallic alloy nanoparticles encapsulated within N-doped graphene as robust bifunctional electrocatalysts for overall water splitting, *Nano Energy* 50 (2018) 212–219.
- [45] L. Ji, J. Wang, X. Teng, H. Dong, X. He, Z. Chen, N,P-Doped molybdenum carbide nanofibers for efficient hydrogen production, *ACS Appl. Mater. Interfaces* 10 (2018) 14632–14640.
- [46] Y.Y. Chen, Y. Zhang, W.J. Jiang, X. Zhang, Z. Dai, L.J. Wan, J.S. Hu, Pomegranate-like N,P-Doped Mo₂C@C nanospheres as highly active electrocatalysts for alkaline hydrogen evolution, *ACS Nano* 10 (2016) 8851–8860.
- [47] W. Zhou, T. Xiong, C. Shi, J. Zhou, K. Zhou, N. Zhu, L. Li, Z. Tang, S. Chen, Bioreduction of precious metals by microorganism: efficient Gold@N-doped carbon

electrocatalysts for the hydrogen evolution reaction, *Angew. Chem. Int. Ed.* 55 (2016) 8416–8420.

[48] J. Qiu, Z. Yang, Q. Li, Y. Li, X. Wu, C. Qi, Q. Qiao, Formation of N-doped molybdenum carbide confined in hierarchical and hollow carbon nitride microspheres with enhanced sodium storage properties, *J. Mater. Chem. A* 4 (2016) 13296–13306.

[49] Y. Li, K. Yin, L. Wang, X. Lu, Y. Zhang, Y. Liu, D. Yan, Y. Song, S. Luo, Engineering MoS_2 nanomesh with holes and lattice defects for highly active hydrogen evolution reaction, *Appl. Catal. B-Environ.* 239 (2018) 537–544.

[50] J. Liu, Y. Liu, D. Xu, Y. Zhu, W. Peng, Y. Li, F. Zhang, X. Fan, Hierarchical “nanoroll” like $\text{MoS}_2/\text{Ti}_3\text{C}_2\text{T}_x$ hybrid with high electrocatalytic hydrogen evolution activity, *Appl. Catal. B-Environ.* 241 (2019) 89–94.

[51] Z. Pu, S. Wei, Z. Chen, S. Mu, Flexible molybdenum phosphide nanosheet array electrodes for hydrogen evolution reaction in a wide pH range, *Appl. Catal. B-Environ.* 196 (2016) 193–198.

[52] D. Wang, X. Zhang, S. Bao, Z. Zhang, H. Fei, Z. Wu, Phase engineering of a multiphasic 1T/2H MoS_2 catalyst for highly efficient hydrogen evolution, *J. Mater. Chem. A* 5 (2017) 2681–2688.

[53] Y. Yang, W. Zhang, Y. Xiao, Z. Shi, X. Cao, Y. Tang, Q. Gao, CoNiSe_2 heteronanoanorods decorated with layered-double-hydroxides for efficient hydrogen evolution, *Appl. Catal. B-Environ.* 242 (2019) 132–139.

[54] P. Sudhagar, N. Roy, R. Vedarajan, A. Devadoss, C. Terashima, K. Nakata, A. Fujishima, Hydrogen and CO_2 reduction reactions: mechanisms and catalysts, in: S. Giménez, J. Bisquert (Eds.), *Photoelectrochemical Solar Fuel Production: From Basic Principles to Advanced Devices*, Springer International Publishing, Cham, 2016, pp. 105–160.

[55] Y. Li, H. Wang, L. Xie, Y. Liang, G. Hong, H. Dai, MoS_2 nanoparticles grown on graphene: an advanced catalyst for the hydrogen evolution reaction, *J. Am. Chem. Soc.* 133 (2011) 7296–7299.

[56] J. Xie, H. Zhang, S. Li, R. Wang, X. Sun, M. Zhou, J. Zhou, W. Lou Xiong, Y. Xie, Defect-rich MoS_2 ultrathin nanosheets with additional active edge sites for enhanced electrocatalytic hydrogen evolution, *Adv. Mater.* 25 (2013) 5807–5813.

[57] Y. Yin, J. Han, Y. Zhang, X. Zhang, P. Xu, Q. Yuan, L. Samad, X. Wang, Y. Wang, Z. Zhang, P. Zhang, X. Cao, B. Song, S. Jin, Contributions of phase, sulfur vacancies, and edges to the hydrogen evolution reaction catalytic activity of porous molybdenum disulfide nanosheets, *J. Am. Chem. Soc.* 138 (2016) 7965–7972.